Sensors and Actuators A 251 (2016) 108–118

Contents lists available at ScienceDirect

Sensors and Actuators A: Physical

journal homepage: www.elsevier.com/locate/sna

A miniature circular pump with a piezoelectric bimorph and a disposable chamber for biomedical applications

H.K. Ma [a,*], R.H. Chen [a], N.S. Yu [a], Y.H. Hsu [b]

[a] *Department of Mechanical Engineering, National Taiwan University, Taipei, Taiwan*
[b] *Institute of Applied Mechanics, National Taiwan University, Taipei, Taiwan*

ARTICLE INFO

Article history:
Received 3 May 2016
Received in revised form 4 October 2016
Accepted 9 October 2016
Available online 11 October 2016

Keyword:
Disposable pump
Piezoelectric bimorph pump
Biomedical fluid transmission

ABSTRACT

Piezoelectric miniature pumps provide excellent stability and accuracy, and thus, have been used in fluid handling and medical applications. In the current study, a separable piezoelectric miniature pump was developed by combining a piezoelectric bimorph actuator and a disposable pumping chamber. By employing a single-use disposable pumping chamber the cross-contamination issues caused by repeated uses of the pumping chamber can be easily avoided, making the pump ideal for biological fluid transmission process. The pumping in the proposed miniature pump was indirectly driven by a circular piezoelectric bimorph actuator through a pillar structure that connects the actuator with the covering PET diaphragm of the pumping chamber. The pumping efficiency of the proposed miniature pump was investigated with respect to several parameters, such as the diaphragm thickness, the chamber diameter and the pillar-to-chamber ratio. A maximum flow rate of 9.1 mL/min was achieved by using the proposed pump structure with 10 mm chamber diameter and a pillar-to-chamber ratio of 0.9.

1. Introduction

Miniature pumps are important due to their wide usage in fluidic applications, such as medical micro scale infusion [1], fuel cells [2], and heat dissipation systems [3]. The infusion pumps are used in fluid infusion for high accuracy and stable transmission for drug delivery [4,5]. Particularly, infusion pumps actuated by magnetic metal alloy material has been widely investigated, and in this regard, a fine flow control of 1–50 μL/s was achieved by controlling the movement of magnetic materials with a varied polarity [6–8].

Miniature and micropumps based on piezoelectric (PZT) ceramics, such as Lead Zirconate Tridentate, have also been widely applied and commercialized for biomedical applications. These pumps can be classified into two categories: pumps with valve, and valveless pumps [9–13]. Typical commercially available biomedical piezoelectric infusion pumps are valve-controlled and have flow rates ranging from a few mL/min to a few tens of mL/min. For example, Microbase's piezoelectric diaphragm pumps have flow rates of 3 mL/min and 15 mL/min, Microjet Liquid's micropump model PS15L has flow rates of 10 mL/min and 50 mL/min, and Bartels*m*$^{\text{ikrotechnik}}$ micropumps have flow rate of 5 mL/min and 7 mL/min. The main advantages of using piezoelectric materials in pumps are easy assembling, low energy consumption, and low cost. However, for biomedical applications, the presence of valves poses more challenges in product certification and cost since biocompatible materials are required in such applications. Furthermore, in medical applications, all parts of a miniature pump in contact with a patient's body fluids must be disposed. In this regard, if any toxic heavy metal is presented in the pumping system, disposal of the pump can cause considerable environmental problems, and the cost of disposal is considerably high. Thus, most of the active components of medical pumps are usually designed as separate pumping units and a piping system is used to connect to the interfacing chamber. This makes biomedical pumping unit bulky, such as quantitative infusion pump and blood pump. Some examples of bulky pumping systems are quantitative anesthesia DAIKEN Coopdech Syringe Pump, quantitative drip IRADIEM Mridium$^{\text{TM}}$ 3860^{+} MRI IV pump and blood infusion pump GE Healthcare enFlow system.

For biomedical applications, a valveless pump can minimize the issues of biocompatibility and waste disposal. A detailed review on valveless micropumps and their designs based on MENS technology has been described by Nguyen et al. [14]. Among the valveless pumps, nozzle/diffuser is one of the simplest designs to be integrated with a mechanical actuator. Stemme et al. [15] were the first to adopt nozzles in place of valves. In their study, micropumps using nozzles/diffusers with $2\theta = 5.3^\circ$ and 10.7° were fabricated and tested. The design was based on a 19 mm circular pumping chamber with a 16 mm circular PZT actuator, and the nozzle/diffuser acted as fluid inlet and outlet. A maximum flow rate of 16 mL/min

* Corresponding author.
E-mail addresses: skma@ntu.edu.tw, hkma78@gmail.com (H.K. Ma).

http://dx.doi.org/10.1016/j.sna.2016.10.010
0924-4247/

and maximum back pressure of 19.6 kPa were obtained. This result demonstrated the potential to commercialize PZT miniature pumps in biomedical fields.

Following Stemme et al., a lot of studies have been focused on the design of valveless pumps. For example, Ulmann [16] studied the correlation and theoretical background of the converging inlets and outlets. Jiang et al. [17] studied the micro nozzle/diffuser flow with different Reynolds numbers (*Re*) and conical angles. The performance of the pump with different conical angle α and corresponding flow resistance of the nozzle/diffuser were evaluated. The experimental results showed that the flow resistance at the outlet was larger than the flow resistance at the inlet with α (2θ) ranging from 5° to 10°, and a flow rate of 0.28 mL/min was achieved at 50 mW and 500 Hz. Olsson et al. [18] studied performance of two valveless pumps in series by using finite element method. They demonstrated that with the two pumps working out of phase, a maximum flow rate of 1.2 mL/min can be reached with a back pressure of 100 kPa. Dinh and Ogami [19] used finite element method and found that the performance of micropumps is a function of damping. Nguyen et al. [20] proposed a valveless pump fabricated via printed circuit board (PCB) technology, providing the advantages of low cost and production flexibility. A maximum flow rate of 3 mL/min was achieved. Singh et al. [21] studied a valveless pump using both numerical simulation and real system test. The numerical simulations were performed to study the effects of nozzle angle/size, chamber diameter/height and membrane diameter/thickness on the flow rate. A maximum flow rate of 0.02 mL/min was achieved at a driving voltage of 30 V and back pressure of 220 Pa. Kumar et al. [22] studied valveless pumps with single and multiple nozzle/diffuser inlets and outlets. A two inlet-two outlet micropump was reported to provide a maximum flow rate of 0.336 mL/min at 5 V, 20 Hz and a maximum back pressure of 441 Pa.

Apart from the design and influence of nozzle/diffuser configuration, chamber design and PZT actuator should also be taken into account in the design of a valveless pump. For example, some researches explored the shape and size of the pumping chamber with the purpose to enhance the pumping performance [23–29]. On the other hand, it has been demonstrated experimentally and numerically that a bimorph PZT actuator can provide a higher actuating force than a unimorph PZT actuator [30,31].

To meet the requirements of biomedical applications, the aim of the current study is to develop a miniature piezoelectric pump having a disposable pumping chamber to handle body fluids of patients. The pumping chamber was designed in such a way so that it can be easily assembled and disposed. A valveless pump made by a circular-shaped plastic pumping chamber was designed to enable an effective assembly with a circular piezoelectric bimorph actuator. This design would significantly reduce the overall cost of the medical pumps since only the pumping chamber is in contact with body fluids of patients and needs to be discarded. Furthermore, using a circular piezoelectric bimorph to directly interface with the pumping chamber, the overall volume of the miniature pump can be reduced to a miniature size. The size of the entire pump was 40 mm in width by 40 mm in length by 10 mm in height, and the disposable chamber was only 40 mm wide by 40 mm long by 2 mm height.

2. Development of a miniature circular pump with a disposable chamber

2.1. Design concept

Fig. 1(a), (b) and (c) show the design of the proposed miniature circular pump and the disposable chamber assembly, respectively. The pump comprised a bimorph PZT actuator and a pumping chamber Fig. 1(a). The bimorph PZT actuator was composed of two Lead Zirconate Titanate pieces attached to brass disk carrier. The pumping chamber was made of a Poly-methyl-methacrylate (PMMA) block machined by a computer-numerical-controlled (CNC) milling machine. The miniature circular pump was 40 mm long, 40 mm wide and 10 mm in height. The sizes of the outlet nozzle and the inlet diffuser were identical with 3.6 mm diameter, 4.7 mm length and angle of 10°. The nozzle and the diffuser were made separately and assembled to the opposite sides of the pumping chamber. The larger opening of the inlet diffuser was pointed toward the pumping chamber, while that of the outlet nozzle was pointed out of the pump. A 27 mm in diameter circular piezoelectric bimorph composed of a 0.2 mm thick brass carrier was sandwiched by two 0.2 mm thick piezoelectric layers with 20 mm diameter. The diaphragm was made of a Polyethylene Terephthalate (PET) sheet. The physical contact between the bimorph PZT actuator and the diaphragm was through a 7 mm high pillar. The pillar was able to transfer force and vibration of circular bimorph PZT to the PET diaphragm. Silicone O-rings with inner diameter of 26 mm and thickness of 1 mm were placed between layers, and screws are used to seal the assembly.

Fig. 1(b) shows the nozzle/diffuser structure. Valveless pumps with various nozzle/diffuser structures had already been reported [32]. However, for portable biomedical applications, a flat pump design is more suitable where the nozzle/diffuser are placed on the sides of the pumping chamber. In addition, since the main purpose of the current study is to explore the feasibility of separable pump design, we simply referred to the studies of Stemme et al. [15] and Jiang et al. [17] to choose a working nozzle/diffuser angle of 10°, which already demonstrated excellent performance.

Fig. 1(c) shows the pumping mechanism of the disposable pump. The voltage-driven oscillation of the bimorph PZT device created a cyclic displacement. As the bimorph PZT actuator moved upward, the diaphragm bounced back with the pillar due to elastic tension. The liquid flowed into the chamber through both the inlet and the outlet. Since a diffuser (left) has a higher flow resistance, the volume flow rate at the inlet was higher than that at the outlet, causing the net volume flow to move into the chamber. As the bimorph PZT actuator moved downward, the diaphragm was pushed downward by the pillar, and the liquid inside the chamber flowed more toward the outlet since a nozzle possesses a lower flow resistance.

To study the performance of the miniature circular pump in converting mechanical vibration through the pillar and the diaphragm, the sizes of the pumping chamber and the pillar were varied and the flow rates were monitored. The parameters tested are shown in Fig. 2. They are the diameter $\boldsymbol{D_c}$ and depth $\boldsymbol{H_c}$ of the disposable chamber, and the diameter $\boldsymbol{D_p}$ and height $\boldsymbol{H_p}$ of the pillar. The depth $\boldsymbol{H_c}$ of the disposable chamber was fixed at 1.5 mm, and three different diameters ($\boldsymbol{D_c}$), viz. 10 mm, 15 mm and 26 mm were studied. The height $\boldsymbol{H_p}$ of the pillar was fixed at 7 mm, and the diameter $\boldsymbol{D_p}$ was varied as 4 mm, 6 mm and 10.6 mm. To quantify the correlation between the pillar and the diaphragm, the ratio $\boldsymbol{S = (D_p/D_c)}$ between the diameters of the pillar to that of the disposable chamber was used. Three conditions were studied, they are $\boldsymbol{S}$ = 0.4, 0.6 and 0.9. Also, the distance between the edges of the pillar to the wall of the disposable chamber (***L***) was used to quantify the area which was not in direct contact with the pillar. Table 1 lists all the experimental conditions.

2.2. Design of the circular bimorph piezoelectric actuator

In order to accommodate the force needed by the disposable chamber, we used bimorph design rather than unimorph structure of the piezoelectric actuator [33]. The bimorph actuator was a three-layered structure composed of a brass carrier with two piezoelectric layers on each surface. The brass carrier was a passive

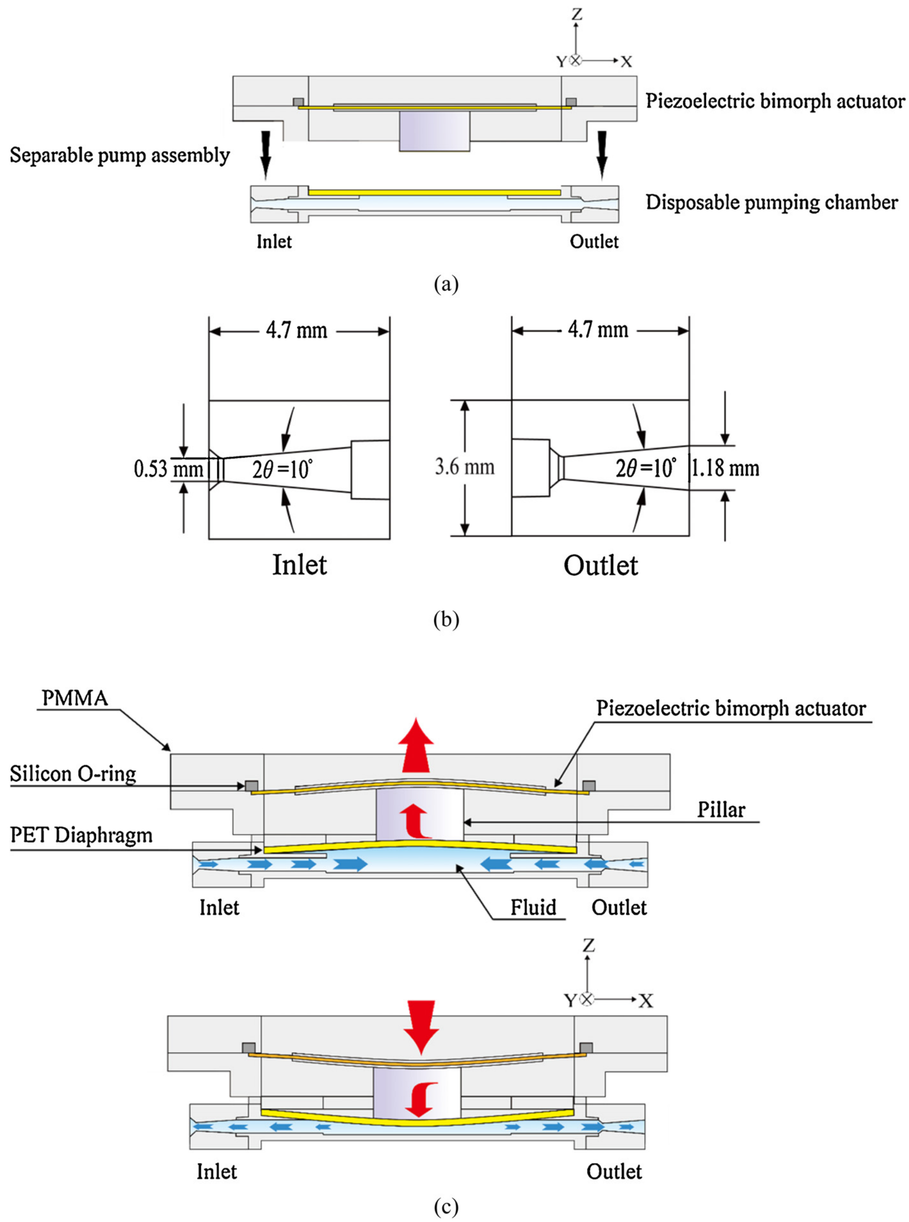

Fig. 1. Structure of a circular miniature pump- (a) separable assembly of disposable pumping chamber and piezoelectric bimorph actuator, (b) a schematic view of nozzle/diffuser structure, and (c) cross-sectional view of pumping operation.

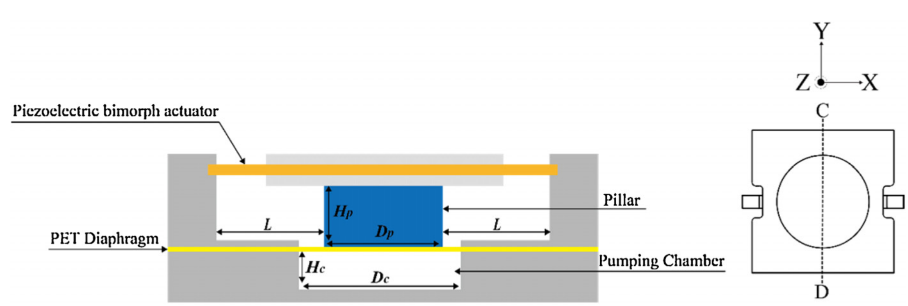

Fig. 2. Cross-sectional view and top view of the disposable pumping chamber.

component that was bound to the piezoelectric layers using epoxy, as shown in Fig. 3. The deformation of the actuator is related to its inner stress distribution, whose force balance must be satisfied under deformation. The thickness of epoxy was much thinner than the PZT layer and the brass carrier, and thus, was ignored in this model. From the formula of total stress shown below [34]:

$$\sum F_x = 0 = \int \sigma_x dA \tag{1}$$

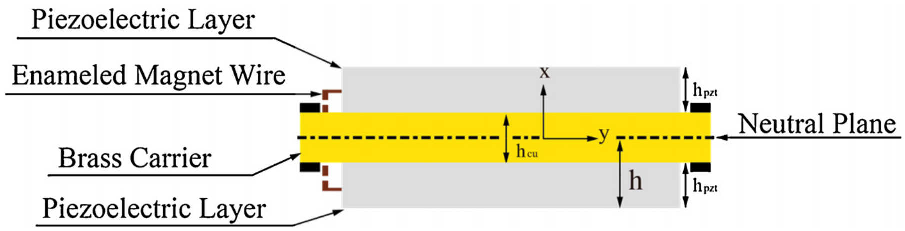

Fig. 3. Piezoelectric bimorph actuator using a brass carrier.

Table 1
Structural parameters used in the experiments.

Pillar Ratio (S)	Chamber Diameter, D_c (mm)	Pillar Diameter, D_P (mm)	L (mm)
0.4	10	4	3
	15	6	4.5
	26	10.4	7.8
0.6	10	6	2
	15	9	3
	26	15.6	5.2
0.9	10	9	0.5
	15	13.5	0.75
	26	23.4	1.3

It can be deducted that

$$\int_{-h}^{-h+h_{pzt}} \sigma_{pzt} dA + \int_{-h+h_{pzt}}^{h-h_{pzt}} \sigma_{cu} dA + \int_{h-h_{pzt}}^{h} \sigma_{pzt} dA = 0 \quad (2)$$

where σ_{cu}, σ_{pzt}, h_{cu} and h_{pzt} represent the inner stress of brass carrier, the inner stress of piezoelectric layer, the thickness of brass carrier and the thickness of piezoelectric layer, respectively. The parameter $\boldsymbol{h}$ represents the distance from neutral plane to the top and bottom of the piezoelectric layer in the three-layered structure, which can be deduced from the material size and properties. The relationship is shown below:

$$h = h_{pzt} + \frac{1}{2} h_{cu} \quad (3)$$

Based on plate theory [34], the stress and strain of piezoelectric materials can be deduced, as shown in Eq. (4) and Eq. (5)

$$\varepsilon(Z) = \varepsilon_{pzt} = \varepsilon_{cu} = Z\kappa \quad (4)$$

$$\sigma_{cu} = \frac{E_{cu} Z}{1 - \nu_{Cu}^2} \quad (5)$$

where ε_{pzt} and ε_{cu} are the inner strain of the piezoelectric layer and the brass carrier, respectively. The parameter κ represents the radius of curvature of the bending plate. Since PZT is a transversely isotropic material and the bimorph structure is symmetric, from the liner piezoelectric constitutive equations [35], the stress and strain relationship for the PZT-actuator can be expressed as

$$\sigma_{pzt} = \frac{E_{pzt} Z}{1 - \nu_{pzt}^2} \left(\kappa Z - \frac{V d_{31}}{h_{pzt}} \right) = \frac{E_{pzt} \kappa Z^2}{1 - \nu_{pzt}^2} - \frac{E_{pzt} V d_{31} Z}{h_{pzt} \left(1 - \nu_{pzt}^2\right)} \quad (6)$$

where ν_{cu} and ν_{pzt} are the poison ratios of the brass carrier and the piezoelectric layer, respectively. E_{cu} and E_{pzt} are the Young's Modulus of the brass carrier and the piezoelectric layer, respectively. $\boldsymbol{d_{31}}$ is the piezoelectric charge constant and $\boldsymbol{V}$ is the applied voltage. Finally, the resultant moment gives

$$N = \int_{-h}^{-h+h_{pzt}} \sigma_{pzt} Z_{pzt} dz + \int_{-h+h_{pzt}}^{h-h_{pzt}} \sigma_{cu} Z_{cu} dz + \int_{h-h_{pzt}}^{h} \sigma_{pzt} Z_{pzt} dz \quad (7)$$

Table 2
Piezoelectric bimorph component parameters.

Elements	Value
PZT Young's modulus	5.20×10^{10}
PZT Poisson's ratio, ν	0.31
PZT d_{31} (m/v)	-2.10×10^{-10}
PZT Density (kg/m^3)	7.78
Brass Young's modulus	1.03×10^{10}
Brass Poisson's ratio, ν	0.33
PET Density (kg/m^3)	920
PET Young's modulus	1.01×10^{10}
PET Poisson's ratio, ν	0.4

Table 3
Calculated results for different brass carrier thickness.

Parameters	Thickness (mm)	Neutral Plane	Moment	Kappa
Brass carrier	0.15	2.75×10^{-4}	5.92×10^{-1}	1.7×10^{-1}
	0.2	3×10^{-4}	6.8×10^{-1}	1.5×10^{-1}
	0.25	3.25×10^{-4}	7.6×10^{-1}	1.3×10^{-1}
Piezoelectric layer	0.2			

Substituting Eqs. (5) and (6) in Eq. (7) leads to:

$$N = \int_{-h}^{-h+h_{pzt}} \left(\frac{E_{pzt} \kappa Z_{pzt}}{1 - \nu_{pzt}^2} - \frac{E_{pzt} V d_{31}}{h_{pzt} \left(1 - \nu_{pzt}^2\right)} \right) Z_{pzt} dz + \int_{-h+h_{pzt}}^{h-h_{pzt}} \frac{E_{cu} \kappa}{1 - \nu_{Cu}^2 Z^2{}_{cu}} dz + \int_{h-h_{pzt}}^{h} \left(\frac{E_{pzt} \kappa Z_{pzt}}{1 - \nu_{pzt}^2} + \frac{E_{pzt} V d_{31}}{h_{pzt} \left(1 - \nu_{pzt}^2\right)} \right) Z_{pzt} dz = 0 \quad (8)$$

Thus, the moment for circular piezoelectric bimorph can be written as

$$\frac{E_{pzt} V d_{31} \left(h_{pzt}^2 - 2hh_{pzt}\right)}{h_{pzt} \left(1 - \nu_{pzt}^2\right)} = \frac{2}{3} \left[\frac{E_{pzt} \left(-3hh_{pzt}^2 + h_{pzt}^3\right)}{\left(1 - \nu_{pzt}^2\right)} + \frac{E_{Cu} \left(h^3 + 3h^2 h_{pzt} - h_{pzt}^3\right)}{\left(1 - \nu_{cu}^2\right)} \right] \kappa \quad (9)$$

By using the parameters provided by PZT vendors (listed in Table 2) and putting them into Eq. (9), the moment $\boldsymbol{N}$ can be calculated. Table 3 lists the calculated moment $\boldsymbol{N}$ and curvature radius $\boldsymbol{\kappa}$ with different piezoelectric layer thickness h_{pzt}, calculated from Eqs. (5) and (9). It was clearly revealed that the piezoelectric bimorph moment $\boldsymbol{N}$ and curvature radius $\boldsymbol{\kappa}$ are functions of the piezoelectric layer thickness h_{pzt}. Based on the results of the previous study [32], a thinner PZT disk has a larger $\boldsymbol{\kappa}$ and can provide larger vibrating amplitude; however, limited by the material sources, the thinnest PZT disk that this study could access was 0.2 mm. Therefore, two 0.2 mm thick PZT (h_{pzt}) disks were used to form the bimorph PZT actuator in order to realize the highest pumping strength for this miniature pump system.

2.3. Effect of the diaphragm and the pillar on the pump performance

To understand the effect of the diaphragm and the pillar on the pumping performance, a lumped spring-mass-damper system (***MCK)*** model was developed, where $F_{input}(\sin\omega t)$ represents the external force applied to the miniature pump system, ***M*** is the total equivalent mass of the miniature pump system, ***C*** is the equivalent damper, ***K*** is the equivalent elasticity coefficient. ***X*** represents the dynamic amplitude of the PET diaphragm, driven by the oscillation of the piezoelectric bimorph actuator.

Fig. 4 shows the oscillatory system of the miniature pump without a pumping fluid. It can be modeled as a standard ***MCK*** model and written as Eq. (11):

$$F_{input}(\sin\omega t) = M\ddot{X} + C\dot{X} + KX, \tag{11}$$

where $F_{input}(\sin\omega t)$ represents the external force applied to the miniature pumping system, and total mass ***M*** is the summation of piezoelectric bimorph (m_{pzt}), diaphragm and pillar ($m_{pillar+diaphragm}$). The total spring coefficient ***K*** comprises contributions from the spring coefficients k_{pzt} and $k_{pillar+diaphragm}$ connected in parallel. Similarly, the total damper ***C*** comprises the contributions from the damping effects of piezoelectric bimorph C_{pzt} and pillar, and diaphragm ($C_{pillar+diaphragm}$)connected in parallel. Thus, this lumped ***MCK*** system can be written as:

$$F_{input}(\sin\omega t) = \left(M_{pzt} + M_{pillar+diaphragm}\right)\ddot{X} + \left(\frac{C_{pzt}C_{pillar+diaphragm}}{C_{pzt} + C_{pillar+diaphragm}}\right)\dot{X} + \left(K_{pzt} + K_{pillar+diaphragm}\right)X \tag{12}$$

Solving Eq. (12) by using the Laplace transform, the diaphragm displacement *X(s)* can be written as Eq. (13).

$$X(s) = \frac{F_{input}(\sin\omega t)}{\left(M_{pzt} + M_{pillar+diaphragm}\right)s^2 + \left(\frac{C_{pzt}C_{pillar+diaphragm}}{C_{pzt}+C_{pillar+diaphragm}}\right)s + \left(K_{pzt} + K_{pillar+diaphragm}\right)} \tag{13}$$

where $\boldsymbol{s} = j\omega$ is the complex angular frequency.

From Eq. (12) and Eq. (13), it was clear that displacement of the PET diaphragm was driven by the piezoelectric actuation and was a function of the driving frequency. Thus, the frequency response of this system, after substituting ***s*** with $j\omega$, can be written as [36]

$$\frac{X}{F}(j\omega) = \frac{1}{\left(K - \omega^2 M\right) + j\omega C} \tag{14}$$

To study the frequency response of the proposed pump system under different pillar-to-chamber ratios (***S***), Eq. (14) was further simplified to Eq. (15) and numerical curve fitting was performed.

$$\mathcal{H}(r) = \frac{1}{1 - r^2 + i2\xi r} \tag{15}$$

where $\mathcal{H}(\boldsymbol{r})$ represents the frequency response, $\boldsymbol{r} = \omega/\omega_n$ is dimensionless angular frequency, ω is the driving angular frequency and $\boldsymbol{\omega_n} = \sqrt{K/M}$ is the natural angular frequency of the system; $\boldsymbol{\xi} = C/2\sqrt{MK}$ is the damping ratio and ***C*** is the lumped damping coefficient of the system. The amplitude of $\mathcal{H}(\boldsymbol{r})$ can be written as:

$$|\mathcal{H}(r)| = \frac{1}{\sqrt{\left(1 - r^2\right)^2 + 4\xi^2 r^2}} \tag{16}$$

The damping effect reduced the resonance amplification and the resultant pumping performance. This equation served as the mathematical model in the Matlab® program to calculate resonant frequencies under different pillar-to-chamber ratios. Thus, we were able to determine the loading effects of the pillar and the diaphragm to the piezoelectric bimorph actuator, and the optimal pillar-to-chamber ratio could be identified.

3. Experimental setup

Fig. 5 shows the experimental setup of the miniature circular pump. The function generator (GW INSTEK SFG-2004) generated a sinusoidal signal, which was then amplified to ±70 V peek-to-peek by a power amplifier (AA LAB System LTD. A-303) and sent to the circular piezoelectric bimorph. The fluid inlet and outlet tubes were placed horizontally on the table to establish a zero back pressure system. Water served as the working fluid. The flow rate was quantified by measuring the average increase in the total liquid weight. The flow rates at different driving frequencies were recorded for analyzing the miniature circular pump performance. The driving frequency was varied from 1 Hz to 100 Hz at a 5 Hz increment. Three sets of pumping chamber with different pillar-to-chamber ratio were also developed.

4. Results and discussion

4.1. Effect of the PET diaphragm thickness on the volume flow rate

The main purpose of a piezoelectric bimorph is to create a large deformation to increase the volume flow rate. The level of deformation is a function of film thickness and its composition. From Eqs. (11) to (16), the increase in diaphragm thickness may lead to two competing effects, one is the increase in the system resonance frequency and oscillation amplitude due to an increase in the spring constant ***K***, the other is the decrease in the system resonance frequency and oscillation amplitude due to increase in the damping coefficient ***C***. To explore the effect of the PET diaphragm thickness on the miniature pump, the volume flow rate was measured with all other structural parameters fixed. The pumping chamber diameter was set to 15 mm, and the pillar-to-chamber ratio of ***S*** = 0.6 was chosen. The volume flow rates under three diaphragm thicknesses, 0.05 mm, 0.10 mm and 0.15 mm were measured with the driving frequency sweeping from 1 Hz to 100 Hz at a 5 Hz increment.

In Fig. 6, the maximum volume flow rate for 0.05 mm thick diaphragm was 1.15 mL/min at its resonance frequency around 15 Hz. The maximum flow rates of 0.10 mm and 0.15 mm thick diaphragms were 2.87 mL/min and 2.21 mL/min, respectively, both at around 25 Hz. The 0.10 mm thick diaphragm provided the highest flow rate in this system. The 23% reduction in the flow rate from the 0.10 mm diaphragm to the 0.15 mm diaphragm and similar resonance frequency indicated increased cancelling effects between ***K*** and ***C*** as the diaphragm thickness continued to increase. As the 0.10 mm diaphragm thickness yielded a higher flow rate, the diaphragm thickness of 0.10 mm was chosen for the following studies.

4.2. Effect of pillar-to-chamber ratios on the frequency responses of the unloaded pump

To understand the influence of the diaphragm and the pillar on the pumping efficiency of the piezoelectric bimorph, frequency response of the piezoelectric bimorph actuator was studied with and without loading the diaphragm and the pillar. The frequency response of the piezoelectric bimorph was measured by using the top piezoelectric layer as the driver and the bottom piezoelectric

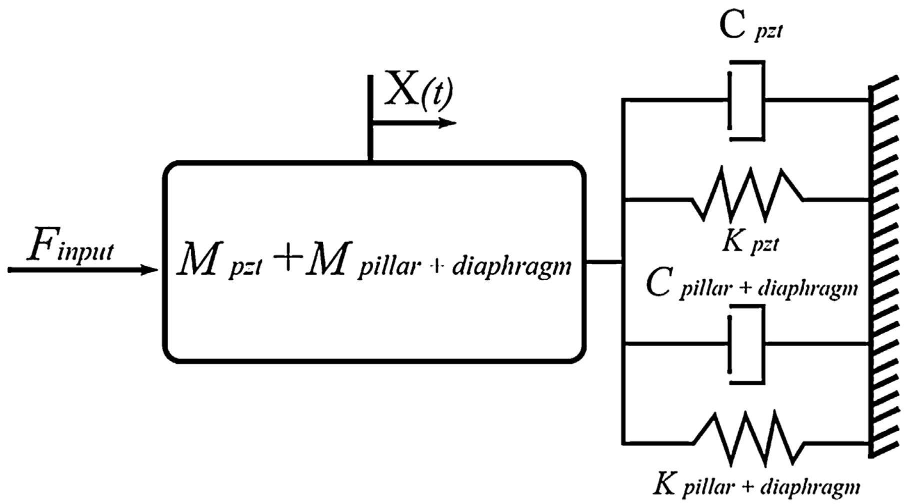

Fig. 4. The equivalent oscillatory system of the piezoelectric bimorph actuator loaded with pillar and diaphragm.

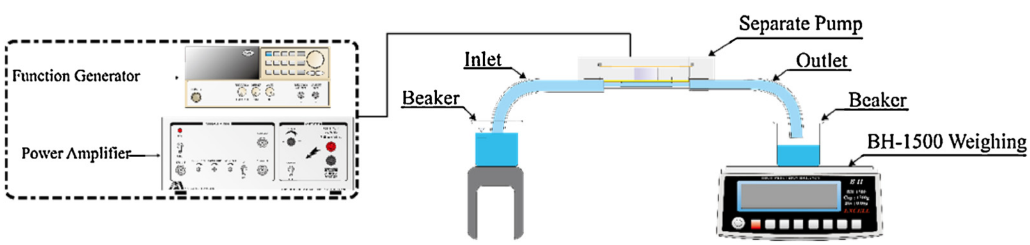

Fig. 5. Experimental setup.

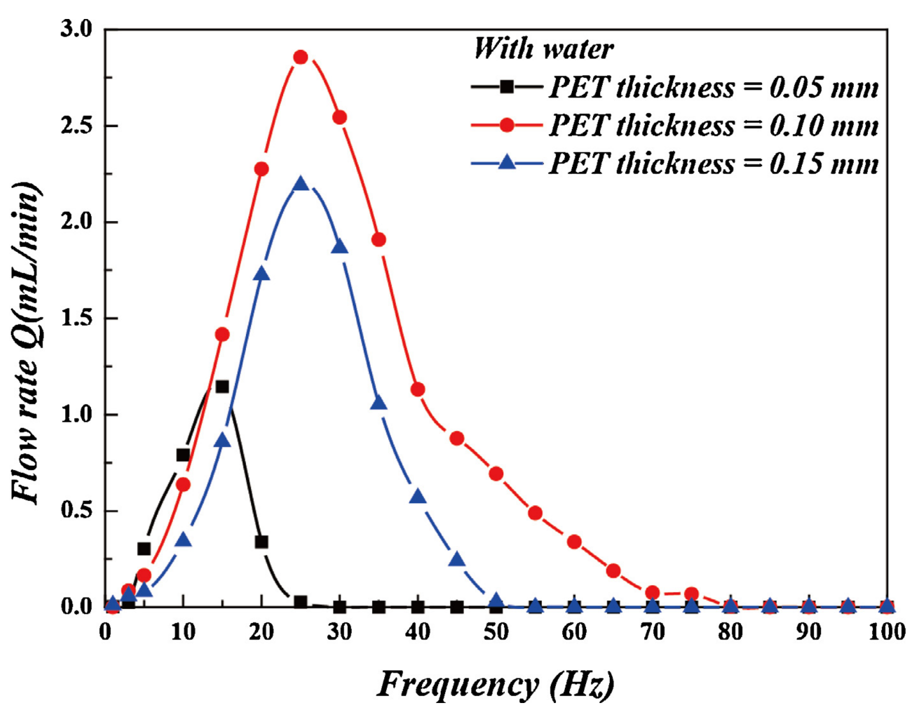

Fig. 6. Measured volume flow rates with frequency under different PET diaphragm thicknesses.

layer as the sensor. An oscilloscope was used to monitor the driving voltage and sensor output. The driving frequency was swept from 1 Hz to 3.5 kHz at an increment of 100 Hz. At frequency range close to the first resonance frequency, a 10 Hz increment was adopted. The ratio between the sensor output and the driver input was also monitored and calculated.

Fig. 7(a) shows the frequency response of the edge-clamped piezoelectric bimorph actuator without loading the pillar and the diaphragm. The resonance frequency was 2.65 kHz. Fig. 7(b), (c) and (d) show the frequency responses of the piezoelectric bimorph actuator assembled with the disposable pumping chamber. Different chamber diameters were adopted, and the pillar-to-chamber

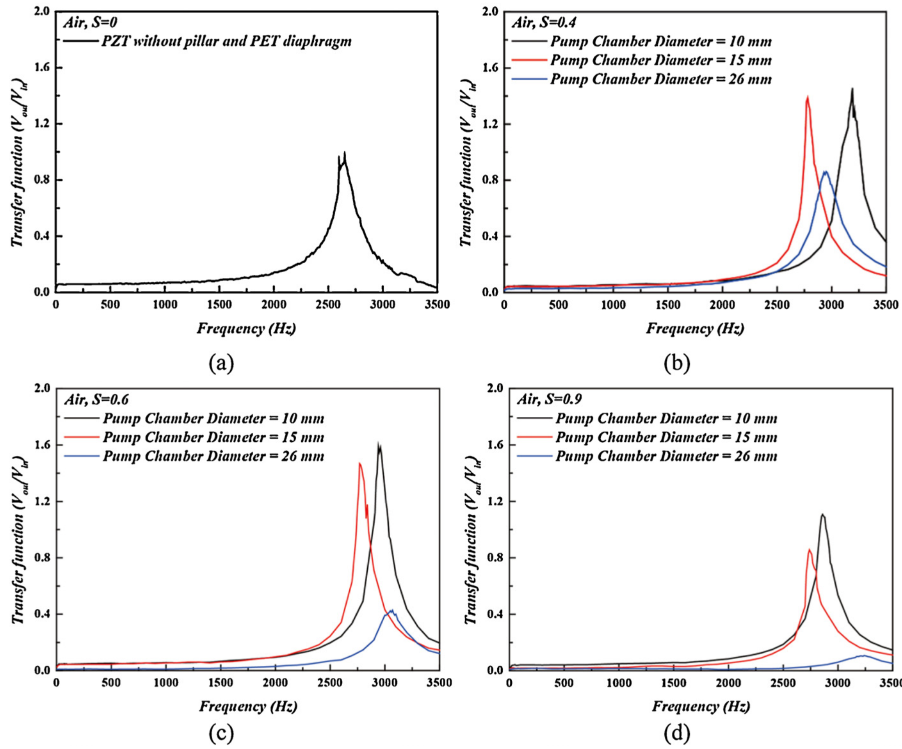

Fig. 7. Variation transfer function with frequency under different pump chamber diameter (a) $\boldsymbol{S}$ = 0 (b) $\boldsymbol{S}$ = 0.4 (c) $\boldsymbol{S}$ = 0.6 (d) $\boldsymbol{S}$ = 0.9.

ratios of $\boldsymbol{S}$ = 0.4, 0.6, and 0.9 were studied. The first resonance under loading showed a slight shift toward higher frequency, ranging from 2.7 kHz to 3.3 kHz. The amplitude at the resonance increased slightly for pumping chambers with 10 mm and 15 mm diameters. Surprisingly, a significant drop was observed in the condition of pumping chamber with 26 mm diameter. This results could be explained by Eqs. (13) and (16). When damping effect was considerable, the resonant frequency and its amplitude decreased significantly. Therefore, to achieve higher oscillation amplitude, a smaller chamber diameter is preferred to avoid excessive damper in the pumping system.

At different pillar-to-chamber ratios $\boldsymbol{S}$, the area of the diaphragm surrounding the pillar could influence the frequency response of the designed pumping system significantly. From Eq. (16) each frequency response was numerically analyzed by using Matlab®, and the fitted resonance frequency and damping ratio $\boldsymbol{\xi}$ were studied. Fig. 8(a) and (b) show the numerically fitted resonance frequencies and damping ratios for different chamber and pillar sizes, respectively. In Fig. 8(a), for chamber diameters of 10 mm (black) and 15 mm (red), the resonance frequencies decreased with increasing $\boldsymbol{S}$, suggesting that the natural frequency ω_n of the system decreased with increasing pillar mass $\boldsymbol{M}$. On the contrary, when the pumping chamber diameter was changed to 26 mm, the resonance frequencies increased with increasing $\boldsymbol{S}$, suggesting that the $\boldsymbol{K}$ component in the natural frequency ω_n of the system started to dominate. This dominance of $\boldsymbol{K}$ can be explained by the much larger elastic diaphragm area around the pillar region.

Fig. 8(b) shows the numerically fitted damping ratios $\boldsymbol{\xi}$ for different chamber sizes and $\boldsymbol{S}$. A clear increasing trend of $\boldsymbol{\xi}$ was observed with increasing $\boldsymbol{S}$ for all the three chamber sizes. Without water in the chamber, the damping mainly came from the interface between the PMMA pillar and the PET diaphragm. By increasing $\boldsymbol{S}$, the interface area between the pillar and the diaphragm was increased, leading to an increased damping ratio. With $\boldsymbol{\xi} = C/2\sqrt{MK}$, the increased $\boldsymbol{\xi}$ agrees with the increased $\boldsymbol{C}$ contributed by the increased interface between the PMMA pillar and the PET diaphragm.

4.3. Effect of pillar-to-chamber ratios on the frequency responses of the water-loaded pump

In order to investigate the influence of chamber diameter and pillar size on the water pumping efficiency, the volume flow rates for different structural parameters (Table 1) were investigated. Fig. 9(a), (b), and (c) show the measured volume flow rate as a function of frequency for three different pillar-to-chamber ratios ($\boldsymbol{S}$ = 0.4, 0.6, and 0.9). The volume flow rates of pumps with different chamber sizes have been represented by the blue (26 mm), red (15 mm), and black (10 mm) lines in each figure. The experimental findings showed that the overall resonant frequencies decreased by two orders of magnitudes due to increased mass loading of water. An optimal volume flow rate of 9.1 mL/min was achieved by using a 10 mm-diameter pumping chamber with a pillar-to-chamber ratio $\boldsymbol{S}$ = 0.9 and a resonant frequency of 70 Hz. The comparison of volume flow rates for different chamber and pillar parameters suggested that a smaller chamber diameter and a higher $\boldsymbol{S}$ lead to higher pumping efficiency and achieves a higher flow rate.

To explain the observed experimental results, the measured volume flow rates with different parameters were also numerically analyzed based on Eq. (16). The resonance frequency and damping ratio $\boldsymbol{\xi}$ of the water-loaded system were identified. Fig. 10(a) and (b) show the numerically fitted resonant frequencies and damping ratios for different chamber and pillar sizes, respectively. In Fig. 10(a), it can be clearly seen that resonant frequency decreased with increasing chamber size. Fig. 10(b) shows that with water loaded in the chamber, the damping ratio was increased by approximately 10 times, and a larger chamber size yielded a larger damping effect. As the chamber size increased, the water mass loading in the pumping chamber also increased along with increased damping due to the increased volume of water, e.g., a 60% increase from

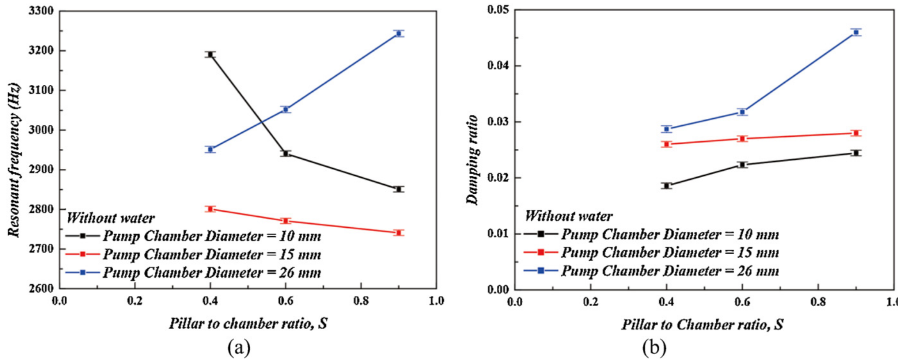

Fig. 8. Comparison of (a) frequency response of different ***S*** with disposable chamber without water, (b) damping ratio of different ***S*** with disposable chamber without water.

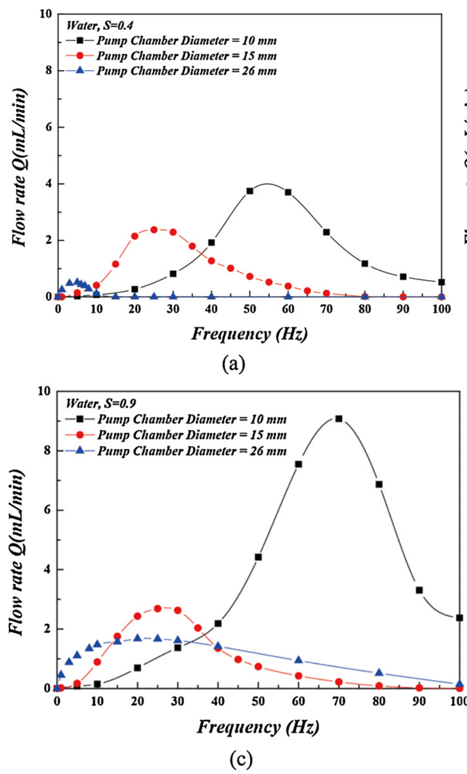

Fig. 9. Variation of volume flow rate with frequency under different pump chamber diameter (a) ***S*** = 0.4 (b) ***S*** = 0.6 (c) ***S*** = 0.9.

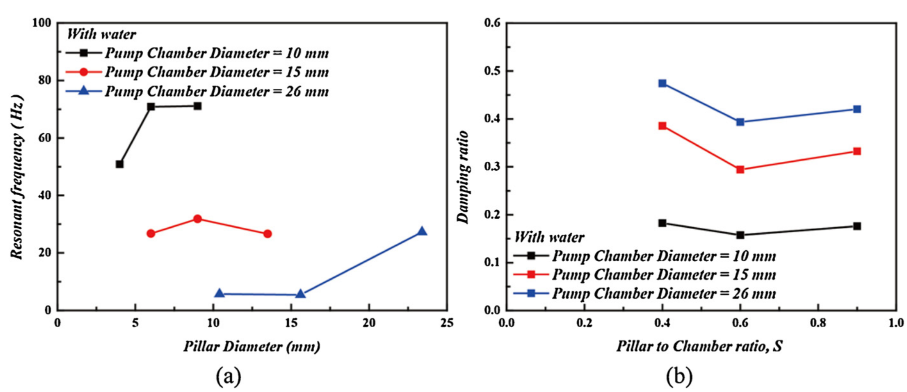

Fig. 10. Comparison of (a) frequency response to different pillar diameter (b) damping ratio of different ***S*** to the disposable chamber of water.

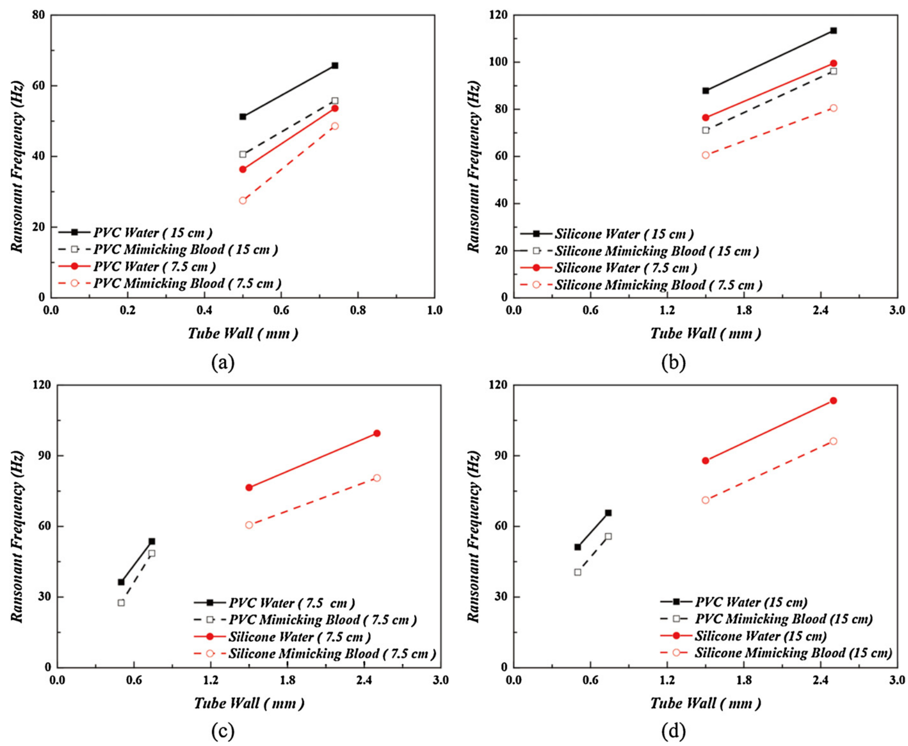

Fig. 11. Plots of frequency responses versus tube wall thickness for (a) different working fluids in PVC tube, (b) different working fluids in silicone tube, (c) PVC and silicone tubes of 15 cm length, and (d) PVC and silicone tubes of 7.5 cm length.

Table 4
Tube parameters used in the experiments.

Material	Inside diameter, I_d (mm)	Outside diameter, O_d (mm)	Wall Thickness (mm)
Silicone	3	6	1.5
	3	8	2.5
PVC	2.8	3.8	0.4
	2.2	3.68	0.74

Table 5
Working fluid parameters used in the experiments.

	Fluid	Density (kg/m^3)	Viscosity (kg/m)
Working fluid	Water	1000	0.0014
	Blood mimicking	1050	0.004

0.2 (chamber diameter 10) to 0.5 (chamber diameter 26) at $\boldsymbol{S}$ = 0.4 in Fig. 10(b). Therefore, the downward shift of resonant frequency with increasing chamber size should be caused by the combined and competing effects of the increased mass loading and increased damping. Careful investigation should be conducted to separate these two competing effects.

4.4. Effect of tube dimension and stiffness on the frequency responses of the fluid-loaded pump

To study the effects of tubing on the frequency response of the pumping system, the pumping system was investigated using different tube materials (PVC and silicone) with different physical parameters (see Table 4), and two different working fluids, viz. water and blood mimic (see Table 5). The tube length was set at 15 cm and 7.5 cm to study the mass loading effect of the working fluids. The chamber size and the pillar-to-chamber ratio were fixed at $\boldsymbol{D_c}$ = 10 mm and $\boldsymbol{S}$ = 0.9, respectively. Fig. 11(a), (b), (c) and (d) show the numerically fitted resonant frequencies against tube wall thickness for both the tube materials with two different lengths. By comparing the frequency responses between 15 cm and 7.5 cm tubes, it was found that the longer tube had a higher resonant frequency, suggesting that under higher mass loading, the resonant frequency shifted to a higher value, e.g. there was a 22% increase from 54 Hz (7.5 cm tube) to 65 Hz (15 cm tube) at PVC wall thickness of 0.74 mm, as shown in Fig. 11(a). By comparing the downward shift of resonant frequency due to the competing mass loading and damping effects of increased water volume, as mentioned in Section 4.3, it can be seen that the water damping effect caused the resonant frequency to shift lower, and for the current pump system, water damping showed a stronger influence on the resonant frequency than the mass loading effect of water.

The silicone tubes with two different outer diameters were used to investigate the effect of thickness on the frequency responses of pumping. The silicone tube with a thicker wall had a higher resonant frequency than the tube with a thinner wall, e.g., there was a 30% increase from 87 Hz (wall thickness 1.5 mm) to 113 Hz (wall thickness 2.5 mm) at silicone tube length of 15 cm, as shown in Fig. 11(b). This observation was in agreement with the hydraulic formula discussion in the previous study [37]. The observation supports that thicker and stiffer tubes have a smaller capacitance effect contributed by the tube expansion under pressure and lead to higher resonant frequencies.

In addition to the changes in tube parameters, two types of working fluids were used to observe the resonant frequency shift with change in viscosity. Comparing the solid (water) and dashed (blood mimic) lines in the four plots in Fig. 11, it can be seen that the fluid higher viscosity yielded lower resonant frequency, e.g. there was a 20% decrease from 100.5 Hz (water) to 80.5 Hz (blood mimic) at silicone tube length of 7.5 cm (see Fig. 11c). Therefore, fluid viscosity has a lowering effect on the resonant frequency of the pump system. As fluid viscosity is correlated with the damping effect of the fluid [38], it can be inferred that fluid damping caused the resonant frequency to shift downward, which is again in agreement with the observation in Section 4.3.

5. Conclusions

An innovative miniature circular pump with a piezoelectric bimorph and a disposable chamber was successfully developed. The performances of pumping chamber under different chamber diameters and pillar-to-chamber ratios were investigated and discussed. The main findings are as follows:

1 The diaphragm thickness and its flexural rigidity could significantly influence the resonance frequency and the volume flow rate. For the case of using a 15 mm-diameter pumping chamber and pillar-to-chamber ratio, $\boldsymbol{S}=0.6$, a 0.10 mm thick diaphragm could provide the largest flow rate of 2.87 mL/min. There was a 23% increase in the flow rate compared to a 0.15 mm thick diaphragm.
2 Loading effects of the proposed pump system were also studied. It was found that the resonant frequency shifted from 2.65 kHz to 3.20 kHz when the piezoelectric bimorph actuator was loaded with the pumping chamber. With water loaded in the pumping chamber, the resonance frequency was further shifted by two orders of magnitude. The loading effects of water included increased mass loading and increased damping effect. This study was able to identify that the damping effect caused the resonant frequency to shift downward, while the mass loading effect led to an increase in resonant frequency of the pump system.
3 The optimal volume flow rate was 9.1 mL/min for 10 mm-diameter pumping chamber and pillar-to-chamber ratio, $\boldsymbol{S}=0.9$ at the resonant frequency of 70 Hz. Based on experimental observations, a small chamber diameter and a large pillar-to-chamber ratio are suggested to achieve a better volume flow rate by using the proposed separable piezoelectric bimorph pump design.
4 Tube wall thickness and stiffness also affected the resonant frequency. As the PVC tube length increased from 7.5 cm to 15 cm, the resonant frequency shifted higher from 54 Hz to 65 Hz. When the silicone tube wall thickness was increased from 1.5 mm to 2.5 mm, the resonant frequency shifted higher from 87 Hz to 113 Hz. Based on these experimental observations, it can be inferred that a longer tube yields higher mass loading and causes the resonant frequency to shift higher, whereas a tube with a thicker/stiffer wall reduces the system capacitance and thus causes the resonant frequency to shift higher.

Acknowledgment

This research was funded by the Ministry of Economic Affairs, R.O.C. (103-EC-19-A-19-S1-225).

References

[1] B. Ma, S. Liu, Z. Gan, G. Liu, X. Cai, H. Zhang, Z. Yang, A PZT insulin pump integrated with a silicon microneedle array for transdermal drug delivery, Microfluid. Nanofluid. 2 (2006) 417–423.
[2] H.K. Ma, S.H. Huang, Y.Z. Kuo, A novel ribbed cathode polar plate design in piezoelectric proton exchange diaphragm fuel cells, J. Power Sources 185 (2008) 1154–1161.
[3] H.K. Ma, B.R. Chen, J.J. Gao, C.Y. Lin, Development of an OAPCP-micropump liquid cooling system in a laptop, Int. Commun. Heat Mass Transf. 36 (2009) 225–232.
[4] H. Gensler, R. Sheybani, P.Y. Li, R.L. Mann, E. Meng Meng, An implantable MEMS micropump system for drug delivery in small animals, Biomed. Microdevices 14 (3) (2012) 483–496.
[5] A. Cobo, R. Sheybani, H. Tu, E. Meng, A wireless implantable micropump for chronic drug infusion against cancer, Sens. Actuator A: Phys. 239 (2016) 18–25.
[6] H. Yu, W. Ye, W. Zhang, Z. Yue, G. Liu, Design, fabrication, and characterization of a valveless magnetic travelling-wave micropump, J. Micromech. Microeng. 25 (2015) 065019.
[7] Y. Wei, R. Torah, K. Yang, S. Beeby, J. Tudor, A novel fabrication process to realize a valveless micropump on a flexible substrate, Smart Mater. Struct. 23 (2014) 025–034.
[8] A.R. Smith, A. Saren, J. Järvinen, K. Ullakko, Characterization of a high-resolution solid-state micropump that can be integrated into microfluidic systems, Microfluid. Nanofluid. 18 (2015) 1255–1263.
[9] A. Azarbadegan, C.A. Cortes-Quiroz, I. Eames, M. Zangeneh, Analysis of double-chamber parallel valveless micropumps, Microfluid. Nanofluid. 9 (2009) 171–180.
[10] Z. Zhang, J. Kan, S. Wang, H. Wang, J. Wen, Z. Ma, Flow rate self-sensing of a pump with double piezoelectric actuators, Mech. Syst. Signal Proc. 41 (2013) 639–648.
[11] T.T. Nguyen, N.S. Goo, V.K. Nguyen, Y. Yoo, S. Park, Design fabrication, and experimental characterization of a flap valve IPMC micropump with a flexibly supported diaphragm, Sens. Actuator A: Phys. 141 (2008) 640–648.
[12] T.Q. Truong, N.T. Nguyen, A polymeric piezoelectric micropump based on lamination technology, J. Micromech. Microeng. 14 (2004) 632–638.
[13] N.T. Nguyen, T.Q. Truong, A fully polymeric micropump with piezoelectric actuator, Sens. Actuate B: Chem. 97 (2004) 137–143.
[14] N.T. Nguyen, X. Huang, T.K. Chuan, MEMS-micropumps: a review, J. Fluids Eng.-Trans. ASME 124 (2) (2002) 384–392.
[15] E. Stemme, G. Stemme, A valveless diffuser/nozzle-based fluid pump, Sens. Actuator A: Phys. 39 (1993) 159–167.
[16] A. Ullmann, The piezoelectric valve-less pump performance enhancement analysis, Sens. Actuator A: Phys. 69 (1998) 97–105.
[17] X. Jiang, Z. Zhou, X. Huang, Y. Li, Y. Yang, C. Liu, Micronozzle/diffuser flow and its application in micro valveless pumps, Sens. Actuator A: Phys. 70 (1998) 81–87.
[18] A.O. Isson, G. Stemme, E. stemme, A numerical design study of the valveless diffuser pump using a lumped-mass model, Microfluid. Nanofluid. 9 (1999) 34.
[19] T.X. Dinh, Y. Ogami, A dynamic model of valveless micropumps with a fluid damping effect, J. Micromech. Microeng. 21 (2011) 115016.
[20] N.T. Nguyen, X.Y. Huang, Miniature valveless pumps based on printed circuit board technique, Sens. Actuator A: Phys. 88 (2001) 104–111.
[21] S. Singh, N. Kumar, D. George, A.K. Sen, Analytical modeling, simulations and experimental studies of a PZT actuated planar valveless PDMS micropump, Sens. Actuator A: Phys. 225 (2015) 81–94.
[22] N. Kumar, D. George, P. Sajeesh, P.V. Manivannan, A.K. Sen, Development of a solenoid actuated planar valveless micropump with single and multiple inlet-outlet arrangements, J. Micromech. Microeng. J. Micromench. Microeng. 26 (2016) 075013.
[23] X.Y. Wang, Y.T. Ma, G.Y. Yan, D. Huang, Z.H. Feng, High flow-rate piezoelectric micropump with two fixed ends polydimethylsiloxane valves and compressible spaces, Sens. Actuator A: Phys. 218 (2014) 94–104.
[24] A.B. Wang, M.C. Hsieh, Unveiling the missing transport mechanism inside the valveless micropump, Lab Chip 12 (2012) 3024–3027.
[25] B.H. Kim, I.C. Kim, Y.J. Kang, J. Ryu, S.J. Lee, Effect of phase shift on optimal operation of serial-connected valveless micropumps, Sens. Actuator A: Phys. 209 (2014) 133–139.
[26] S. Yang, X. He, S. Yuan, J. Zhu, Z. Deng, A valveless piezoelectric micropump with a Coanda jet element, Sens. Actuator A: Phys. 230 (2015) 74–82.
[27] S. Li, S. Chen, Analytical analysis of a circular PZT actuator for valveless micropumps, Sens. Actuator A: Phys. 104 (2003) 151–161.
[28] E. Sayar, B. Farouk, Dynamic analysis of bulk acoustic wave piezoelectric micropumps: effects of inlet-outlet port angles and overall pump size, Proc. IEEE IMECE, USA, 2013, pp.15-21.
[29] H.K. Ma, H.C. Su, J.Y. Wu, Study of an innovative one-sided actuating piezoelectric valveless micropump with a secondary chamber, Sens. Actuator A: Phys. 171 (2011) 297–305.
[30] Y. Yuan, H. Du, X. Xia, Y.R. Wong, Analytical solutions to flexural vibration of slender piezoelectric multilayer cantilevers, Smart Mater. Struct. 23 (2014) 095005.
[31] Q.M. Wang, X.H. Du, B. Xu, Electromechanical coupling and output efficiency of piezoelectric bending actuators, IEEE Trans. Ultrason. Ferroelectr. Freq. Control 46 (1999) 638–646.
[32] M. Nabavi, Steady and unsteady flow analysis in microdiffusers and micropump: a critical review, Microfluid. Nanofluid. 225 (2015) 81–94.
[33] H.K. Ma, R.H. Chen, Y.H. Hsu, Development of a piezoelectric-driven miniature pump for biomedical applications, Sens. Actuator A: Phys. 234 (2015) 23–33.
[34] S.P. Timoshenko, S. Woinowsky-Krieger, Theory of Plates and Shells, McGraw Hill, New York, 1970.
[35] S. Li, S. Chen, Analytical analysis of a circular PZT actuator for valveless micropumps, Sens. Actuator A: Phys. 104 (2003) 151–161.
[36] S.S. Rao, Mechanical Vibrations, fifth ed., Prentice Hall, New York, 2011.
[37] K.W. Oh, K. Lee, B. Ahn, E.P. Furlani, Design of pressure-driven microfluidic networks using electric circuit analogy, Lab Chip 12 (2012) 515–545.
[38] Y. Zhou, F. Amirouhe, Study of fluid damping effects on resonant frequency of an electromagnetically actuated valveless micropump, Int. J. Adv. Manuf. Technol. (2009) 1187–1196.

Biographies

H.K. Ma received his PhD degree from the department of mechanical engineering, University of Illinois at Chicago, in 1985. He was a research engineer for Energy and Environmental Research Co. (Irvine, USA) in 1985–1987. He then joined the faculty of the department of mechanical engineering, National Taiwan University, in 1987.

R.H Chen received his B.S. degree from Nan Jeon University of Science and Technology, Taiwan, in 2008; and received his M.S. degree from Yuan Ze University, Taiwan, in 2010. He is currently a Ph.D. candidate in the Department of Mechanical Engineering, National Taiwan University, Taiwan.He is focused on the piezoelectric materials for novel actuators, particularly piezoelectric micropumps.

N.H. Yu received her M.S. degree from mechanical engineering at National Taiwan University, in 2015. While she was a master student, she joined the Energy and Environment Laboratory which leaded by Professor H.K. Ma to study in heat transfer and fluid mechanics. Her research interest is focused on the novelty design of micro-pump.

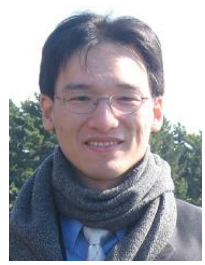

Dr. Yu-Hsiang Hsu is currently an Assistant professor in the Institute of Applied Mechanics and the director of Biomechanical Microsystems Laboratory at National Taiwan University. He received his B.S. degree in Mechanical Engineering and M.S. degree in Applied Mechanics from National Taiwan University in 2000 and 2002, respectively. He then received his M.S. degree and Ph.D. degree in Biomedical Engineering in 2006 and 2010 from the University of California at Irvine. His research interests include biomedical devices, lab-on-a-chip systems, 3D microtissues, and drug screening systems.